North Atlantic Barotropic Vorticity Balances in Numerical Models*

JOSEPH SCHOONOVER

Geophysical Fluid Dynamics Institute, Florida State University, Tallahassee, Florida

WILLIAM DEWAR AND NICOLAS WIENDERS

Department of Earth, Ocean and Atmospheric Sciences, Florida State University, Tallahassee, Florida

JONATHAN GULA, JAMES C. MCWILLIAMS, AND M. JEROEN MOLEMAKER

Department of Atmospheric and Oceanic Sciences, University of California, Los Angeles, Los Angeles, California

SUSAN C. BATES, GOKHAN DANABASOGLU, AND STEPHEN YEAGER

National Center for Atmospheric Research,[+] Boulder, Colorado

(Manuscript received 10 July 2015, in final form 4 November 2015)

ABSTRACT

Numerical simulations are conducted across model platforms and resolutions with a focus on the North Atlantic. Barotropic vorticity diagnostics confirm that the subtropical gyre is characterized by an inviscid balance primarily between the applied wind stress curl and bottom pressure torque. In an area-integrated budget over the Gulf Stream, the northward return flow is balanced by bottom pressure torque. These integrated budgets are shown to be consistent across model platforms and resolution, suggesting that these balances are robust. Two of the simulations, at 100- and 10-km resolutions, produce a more northerly separating Gulf Stream but obtain the correct integrated vorticity balances. In these simulations, viscous torque is nonnegligible on smaller scales, indicating that the separation is linked to the details of the local dynamics. These results are shown to be consistent with a scale analysis argument that suggests that the biharmonic viscous torque in particular is upsetting the inviscid balance in simulations with a more northerly separation. In addition to providing evidence for locally controlled inviscid separation, these results provide motivation to revisit the formulation of subgrid-scale parameterizations in general circulation models.

1. Background

Numerical ocean modeling has reached the stage where global numerical simulations can be conducted at resolutions (≤10 km) that adequately resolve the first baroclinic deformation radius in most locations. Such simulations at the eddy-resolving scale have shown improved western boundary current pathway and separation (Bryan et al. 2007; Chassignet and Marshall 2008; Talandier et al. 2014), though obtaining the correct separation remains a challenging and ad hoc procedure in both global and regional simulations. Climate/earth-system models, such as the Community Earth System Model (CESM), carry additional computational constraints that leave the distraught climate modeler grappling with a coarsely resolved ocean [usually $O(100)$ km]. Despite recent improvements in the ocean component of the CESM, considerable sea surface temperature (SST) biases (up to 7°C) remain because of more northerly separations of western boundary currents, such as the Gulf Stream (Gent et al. 2011).

The reason the Gulf Stream separates consistently at Cape Hatteras remains elusive, though a number of theories have been suggested (Chassignet and Marshall 2008). The classic models of Stommel (1948) and Munk

* Geophysical Fluid Dynamics Institute Contribution Number 474.
[+] The National Center for Atmospheric Research is sponsored by the National Science Foundation.

Corresponding author address: Joseph Schoonover, Geophysical Fluid Dynamics Institute, Florida State University, 77 Chieftan Way, Tallahassee, FL 32306.
E-mail: js08s@my.fsu.edu

DOI: 10.1175/JPO-D-15-0133.1

(1950) predict that western boundary currents separate at the latitude of the zero wind stress curl line for zonal winds. In models that include stratification and bottom topography, Holland (1973) provided scale analysis that argues for an inviscid closure through the presence of bottom pressure torque. Independent of closure, the vorticity input by the wind is exactly balanced along latitudinal lines by an opposing torque generated within the western boundary current. Almost 30 years later, Hughes and DeCuevas (2001) demonstrated in an eddy-permitting primitive equation model that the North Atlantic closure is achieved through bottom pressure torque primarily within the Gulf Stream. At the zero wind stress curl line, the generation of torque and the return transport within the boundary current are no longer required since the interior meridional transport and vorticity input both vanish at this latitude. In this sense, the wind stress curl latitude can be thought of as a global constraint on the separation latitude.

It is true that a western boundary must reconnect with the interior flow that is driven by the wind stress curl. In the Stommel (1948) and Munk (1950) models, the separating boundary current is a result of a boundary layer matching condition coupled with the reversal of the interior Sverdrup transport at the zero wind stress curl line. It is known that sufficient inertia, however, can cause a breakdown of the linear solutions by coupling the boundary layer and the interior flow. This alters the dynamics of the separation process and allows for separation to occur elsewhere (Haidvogel et al. 1992). Additionally, bathymetric features can exert considerable control over the pathways of an oceanic jet like the Gulf Stream (Stern 1998; Hughes 1986). These frameworks emphasize that western boundary currents are not separating from vertical sidewalls, but are instead directly interacting with 3D bathymetry from which they can inevitably separate. In this view, the separation is not constrained by the zero wind stress curl line but is completely controlled by local bathymetric interactions. At some point, though, the separated current must reconnect with the interior flow that leaves room for some degree of control balanced between local and global constraints.

The goal of this paper is to demonstrate the robustness of the inviscid vorticity balance in the subtropical gyre and to provide evidence-based commentary on the importance of local control on the separation of the Gulf Stream. This is done by comparing gyre and western boundary current integrated vorticity budgets from six solutions produced by three distinct general circulation models (GCMs) at a range of resolutions from 100 to 2.5 km. Two of the solutions exhibit a northerly separating Gulf Stream and obtain similar integrated balances to those that show a separation closer to Cape Hatteras. Key differences in these solutions are noted in more local balances within the Gulf Stream. Section 2 introduces the barotropic vorticity budget concept and formalism, and section 3 describes the configuration of the GCMs. The global and local vorticity balances are discussed in section 4.

2. Barotropic vorticity budget

The barotropic vorticity budget is found by taking the vertical component of the curl of the vertically integrated lateral momentum equations:

$$\frac{\partial \overline{\zeta}}{\partial t} = \underbrace{\frac{J(P_b, h)}{\rho_0}}_{\text{(a)}} - \underbrace{\mathscr{A}}_{\text{(b)}} - \underbrace{\nabla \cdot (f\mathbf{U})}_{\text{(c)}} + \underbrace{\frac{\nabla \times \boldsymbol{\tau}_w}{\rho_0}}_{\text{(d)}} - \underbrace{\frac{\nabla \times \boldsymbol{\tau}_b}{\rho_0}}_{\text{(e)}} + \underbrace{\mathscr{D}}_{\text{(f)}}, \tag{1}$$

where $\overline{\zeta} = (\nabla \times \mathbf{U}) \cdot \hat{\mathbf{z}}$ is the barotropic vorticity; $\mathbf{U} = \int_{-h}^{\eta} \mathbf{u}\, dz$ is the lateral transport; $z = -h(x, y)$ defines the bathymetry as a function of lateral position (x, y); $z = \eta(x, y)$ defines the position of the free surface; $P_b = \int_{-h}^{\eta} \rho' g\, dz + \rho_0 g \eta$ is the bottom pressure; g is the acceleration of gravity; ρ' is a density anomaly referenced to a fixed density ρ_0; $\boldsymbol{\tau}_w$ is the applied wind stress at the surface; $\boldsymbol{\tau}_b$ is any bottom stress (e.g.; linear or quadratic drag); $\mathscr{A}$ is the nonlinear torque; and $\mathscr{D}$ represents the viscous torque, which includes the torque introduced by subgrid-scale parameterizations. In order, the underlined terms in the barotropic vorticity budget are referred to as bottom pressure torque (a), nonlinear torque (b), planetary vorticity advection (c), wind stress curl (d), bottom drag curl (e), and viscous torque (f).

To illuminate the meaning of the nonlinear torque, term b is explicitly

$$\mathscr{A} = \nabla \times \left[\int_{-h}^{0} \nabla \cdot (\mathbf{uu})\, dz \right] \cdot \hat{\mathbf{z}} + \nabla \times ([w\mathbf{u}]_{z=-h}^{z=0}). \tag{2}$$

Hereafter, the curl operator $(\nabla\times)$ is representative of the vertical component of the curl operator that yields a scalar. The last term can be expanded into

$$\nabla \times ([w\mathbf{u}]_{z=-h}^{z=0}) = [w\zeta]_{z=-h}^{z=0} - \underline{(w\mathbf{u} \times \nabla h)|_{z=-h}} + [\nabla w \times \mathbf{u}]_{z=-h}^{z=0} - \underline{(w\nabla h \times \mathbf{u})|_{z=-h}}, \tag{3}$$

where the two underlined terms cancel. With this, the nonlinear torque can be written

$$\mathscr{A} = \underbrace{\nabla \times \left[\int_{-h}^{0} \nabla \cdot (\mathbf{uu})\, dz \right]}_{(1)} + \underbrace{[w\zeta]_{z=-h}^{z=0}}_{(2)} + \underbrace{[\nabla w \times \mathbf{u}]_{z=-h}^{z=0}}_{(3)}. \tag{4}$$

Each of the terms in Eq. (4) is referred to as follows: 1) curl of the vertically integrated momentum flux divergence, 2) nonlinear contribution to vortex tube stretching, and 3) transfer of vertical shear to barotropic vorticity. In a time average, the effects of eddies appear in term 1 of Eq. (4) as the curl of vertically integrated divergence of Reynolds stress. To see this, the lateral velocity field is split into a mean and time-varying contribution

$$\mathbf{u} = \langle \mathbf{u} \rangle + \mathbf{u}', \tag{5}$$

where $\langle \cdot \rangle$ denotes a time average. Then, term 1 of Eq. (4) under a time average becomes

$$\left\langle \nabla \times \left[\int_{-h}^{0} \nabla \cdot (\mathbf{uu})\, dz \right] \right\rangle = \nabla \times \left[\int_{-h}^{0} \nabla \cdot (\langle \mathbf{u} \rangle \langle \mathbf{u} \rangle)\, dz \right] + \underline{\nabla \times \left[\int_{-h}^{0} \nabla \cdot (\langle \mathbf{u}'\mathbf{u}' \rangle)\, dz \right]}. \tag{6}$$

The underlined term illustrates the effects of the Reynolds stresses on the barotropic vorticity.

We refer to term c in Eq. (1) as planetary vorticity advection, neglecting vortex tube stretching because the contribution from variability in the free surface is negligible in long time averages. To illustrate this point, vertical integration of the incompressibility condition gives

$$\nabla \cdot \mathbf{U} = -\eta_t, \tag{7}$$

so that term c is equivalent to

$$\nabla \cdot (f\mathbf{U}) = \mathbf{U} \cdot \nabla f - f\eta_t. \tag{8}$$

The latter term is a contribution to vortex tube stretching for a column of fluid. In long time averages, it is assumed that η_t is negligible so that term c is primarily accounted for through planetary vorticity advection and the transport field is essentially divergence-free. In passing it is noted that the bottom pressure torque, under a geostrophic scaling, can be interpreted as vortex tube stretching, though this statement is not true in general (Gula et al. 2015). If geostrophic balance is assumed, then the bottom pressure torque can be written

$$\frac{J(P_b, h)}{\rho_0} = f\mathbf{u}_g \cdot \nabla h = -fw_{\text{bottom}}, \tag{9}$$

where $\mathbf{u}_g$ is the geostrophic velocity at the bottom and w_{bottom} is the vertical velocity associated with the cross isobath flow.

The original models of Stommel (1948) and Munk (1950) describe a wind-driven gyre in terms of steady-state vorticity and mass balances. In these simplified models, integrating over the physical domain is equivalent to integrating over an area enclosed by a barotropic streamfunction contour. Such an integration would yield a bulk vorticity balance for the modeled wind-driven gyre. In a similar manner, a closed barotropic streamfunction contour is chosen to define the subtropical gyre, which also includes the Gulf Stream–North Atlantic current system. An area representative of the Gulf Stream is chosen to lie between two streamfunction contours, beginning just north of the Bahamas at 28°N, and terminating offshore of the separation.

All of the terms shown in Eq. (1) are area-integrated explicitly in application, but here an analytical presentation of the area-integrated budgets is given below. These balances are calculated in order to determine if Sverdrup balance is an appropriate description of the interior North Atlantic subtropical gyre and to verify the robustness of the inviscid closure suggested by Holland (1973) and observed by Hughes and DeCuevas (2001).

a. *Integrated budgets*

In an area integration over a region enclosed by a transport streamfunction contour, planetary vorticity advection plus vortex tube stretching is identically zero since the bounding curve is everywhere tangent to the transport,

$$\int_{\Omega} \nabla \cdot (f\mathbf{U})\, dA = \oint_{\Psi=\text{const}} f\mathbf{U} \cdot \hat{\mathbf{n}}\, dS = 0, \tag{10}$$

with Ω being the region enclosed by Ψ = const. Note that this term is explicitly calculated in the area-averaged budgets here since the divergence theorem identity may be subject to numerical discretization error; it is verified that this error is negligible.

In a time average, it is anticipated that the unsteady terms are unimportant, which leaves the area-integrated budget as (analytically)

$$\int_{\Omega} \left[\frac{J(P_b, h)}{\rho_0} - \mathscr{A} + \frac{\nabla \times \boldsymbol{\tau}_w}{\rho_0} - \frac{\nabla \times \boldsymbol{\tau}_b}{\rho_0} + \mathscr{D} \right] dA = 0. \tag{11}$$

For the region representative of the Gulf Stream, the planetary vorticity advection and vortex tube stretching become

$$\int_\Omega \nabla\cdot(f\mathbf{U})\,dA = (f_{\rm sep} - f_{28^\circ{\rm N}})\Delta\Psi, \tag{12}$$

where $\Delta\Psi$ is the transport of the Gulf Stream. Thus, in order for the Gulf Stream to travel northward the following balance must hold:

$$(f_{\rm sep} - f_{28^\circ{\rm N}})\Delta\Psi = \int_\Omega \left[\frac{J(P_b,h)}{\rho_0} - \mathscr{A} + \frac{\nabla\times\boldsymbol{\tau}_w}{\rho_0} - \frac{\nabla\times\boldsymbol{\tau}_b}{\rho_0} + \mathscr{D}\right] dA. \tag{13}$$

b. Scale analysis

In ocean models that do not achieve reasonable separation, it is anticipated that frictional and viscous effects (both numerical and explicit) may upset local balances within the western boundary current while remaining ‘‘undetected’’ in large-scale diagnostics. In light of recent studies (Hughes 2000; Hughes and DeCuevas 2001; Jackson et al. 2006) it is becoming increasingly evident that the inviscid bottom pressure torque is the primary balance for the wind stress curl in a bulk integrated sense. This is in opposition to the viscous or frictional closures achieved in the classic Stommel (1948) and Munk (1950) models. Here, scale analysis is used to illustrate how local dynamics can differ despite an agreement in large-scale vorticity budgets.

For a current traveling at $V = 1\,{\rm m\,s^{-1}}$ in geostrophic balance at midlatitudes with a cross-stream length scale of L 100 km over a continental slope with a drop-off of $\Delta H \approx 1$ km, the scale for the bottom pressure torque is roughly

$$\left|\frac{J(P_b,h)}{\rho_0}\right| \approx \frac{f_0 V\Delta H}{L} = \frac{(10^{-4}\,{\rm s^{-1}})(1\,{\rm m\,s^{-1}})(1\,{\rm km})}{10^2\,{\rm km}} \approx 10^{-6}\,{\rm m\,s^{-2}}. \tag{14}$$

The lateral viscous torque scales as

$$\left|\nabla\times\int_{-H}^{\eta}\nabla\cdot(A_h\nabla\mathbf{u})\,dz\right| \approx A_h\frac{HV}{L^3} \approx A_h\frac{(1\,{\rm km})(1\,{\rm m\,s^{-1}})}{(10^2\,{\rm km})^3} \approx A_h(10^{-12}\,{\rm m\,s^{-1}}). \tag{15}$$

In order for this term to be comparable to the bottom pressure torque on this length scale, the lateral eddy viscosity would have to be at least $A_h \gtrsim 10^6\,{\rm m^2\,s^{-1}}$.

Assuming the bottom drag is meant to parameterize a momentum flux into an Ekman boundary layer,

$$\frac{\tau_b}{\rho_0} \approx \frac{A_z V}{h_{\rm ek}}, \tag{16}$$

where

$$h_{\rm ek} \approx \sqrt{\frac{A_z}{f}} \tag{17}$$

is the Ekman boundary layer thickness. With this,

$$\left|\frac{\nabla\times\boldsymbol{\tau}_b}{\rho_0}\right| \approx \frac{V\sqrt{A_z f}}{L} \approx \sqrt{A_z}(10^{-7}\,{\rm s^{-3/2}}). \tag{18}$$

This would require a vertical eddy viscosity $A_h \gtrsim 10^2\,{\rm m^2\,s^{-1}}$ in order to compare with the bottom pressure torque. This viscosity coefficient would imply an Ekman boundary layer thickness of $h_{\rm ek} \gtrsim 1$ km, which is on the order of the mean fluid depth and nonsensical.

Since the bottom pressure torque and the bottom drag curl vary like $1/L$, the relative magnitude of these two terms is independent of length scale and should only depend on their ratio,

$$\frac{\left|\dfrac{\nabla\times\boldsymbol{\tau}_b}{\rho_0}\right|}{\left|\dfrac{J(P_b,h)}{\rho_0}\right|} \approx \frac{h_{\rm ek}}{\Delta H}. \tag{19}$$

In regions where ΔH is small, it is possible for the bottom drag curl to overwhelm the bottom pressure torque. The lateral viscous torque, however, can become important for small L, since

$$\frac{\left|\nabla\times\displaystyle\int_{-H}^{0}\nabla\cdot(A_h\nabla\mathbf{u})\,dz\right|}{\left|\dfrac{J(P_b,h)}{\rho_0}\right|} \approx \frac{A_H H}{f\Delta H L^2}. \tag{20}$$

The characteristic length scale for the viscous torque is defined

$$L_{\rm visc} \equiv \left(\frac{A_H H}{f\Delta H}\right)^{1/2}. \tag{21}$$

A similar length scale for a biharmonic viscous torque can be estimated by comparing the bottom pressure and the biharmonic viscous torque:

$$L_{A4} = \left(\frac{A_{4h}}{f}\right)^{1/4}, \tag{22}$$

where A_{4h} is the biharmonic eddy viscosity. For $\Delta H/H \approx O(1)$, $f \approx 10^{-4}\,{\rm s^{-1}}$, $A_h \approx O(10^3)\,{\rm m^2\,s^{-1}}$, and

$A_{4h} \approx O(10^{17})$ m^4 s^{-1}, the viscous torque length scale is approximately $L_{\mathrm{visc}} \approx 3$ km and the biharmonic length scale is $L_{A4} \approx 100$ km. On length scales larger than 100 km, scale analysis suggests that the lateral viscous torque (both Laplacian and biharmonic) become less important as the bottom pressure torque takes over. Note that the values for the Laplacian and biharmonic eddy viscosities are typical for simulations with resolutions of 10 km (see section 3 for the model configurations in this work).

Nonlinear torque compares to the bottom pressure torque like

$$\frac{|\mathscr{A}|}{\left|\dfrac{J(P_b,h)}{\rho_0}\right|} = \frac{V}{fL\dfrac{\Delta H}{H}}, \tag{23}$$

which naturally defines the length scale

$$L_A = \frac{V}{f\dfrac{\Delta H}{H}}. \tag{24}$$

Using the values previously mentioned gives $L_A \approx$ 10 km. Thus, on larger scales, nonlinear torque tends to become less important.

Overall, scale analysis is suggestive of the gyre-scale budgets being closed by a balance of wind stress curl and bottom pressure torque,

$$\int_\Omega \left[\frac{J(P_b,h)}{\rho_0} + \frac{\nabla \times \boldsymbol{\tau}_w}{\rho_0}\right] dA = 0. \tag{25}$$

Further, over the extent of the Gulf Stream along the southeastern U.S. seaboard, up to its separation, it is anticipated that the return flow must be balanced by the bottom pressure torque. This is thought to be the case since the Gulf Stream width and extent are both larger than the characteristic viscous and nonlinear torque length scales, and since $\Delta H > h_{\mathrm{ek}}$ over the continental shelf:

$$(f_{\mathrm{sep}} - f_{28^\circ\mathrm{N}})\Delta\Psi = \int_\Omega \frac{J(P_b,h)}{\rho_0} dA. \tag{26}$$

In short, scale analysis shows how "bulk" or large-scale vorticity balances can be independent of the choice of subgrid-scale closure (viscosity coefficients, drag, etc.), yet the detailed structure of the balances can become sensitive to these choices. Particularly, the ordering of the intrinsic length scales will determine which balances may be realized within the Gulf Stream. Although we anticipate a bulk inviscid closure for the North Atlantic subtropical gyre, it is expected that the detailed balances within the Gulf Stream may be different in each simulation.

TABLE 1. The simulations are shown with their associated resolution and runtime. The runtime refers to the model time that is used in computing the diagnostics and does not include model spinup.

Run name	Resolution	Atmospheric forcing	Run length
POP_C	~100 km	Coupled	10 years
POP_M	~10 km	Imposed stress	3 years
ROMS_M	~6 km	Imposed stress	1 year
MIT_M	~10 km	Calculated stress	10 years
ROMS_F	~2.5 km	Imposed stress	18 years
MIT_F	~3 km	Calculated stress	6 years

3. Model configurations

Three different ocean general circulation models (OGCMs) are used to conduct the numerical simulations, namely, the Parallel Ocean Program (POP; Smith et al. 2010) within the Community Earth System Model, version 1 [CESM1; previously named as the Community Climate System Model, version 4 (CCSM4); Gent et al. 2011], the Regional Ocean Modeling System (ROMS; Shchepetkin and McWilliams 2005), and the Massachusetts Institute of Technology General Circulation Model (MITgcm; Marshall et al. 1997). Three different grid sizes are used, and to distinguish between them the following naming convention is used: "coarse" refers to 100-km nominal resolution, "medium" is ~10 km, and "fine" is ~2.5 km. The POP ocean model simulations are conducted on coarse and medium grids; thus, these two simulations are dubbed POP_C and POP_M. The ROMS and MITgcm simulations use the medium- and fine-resolution grids and are referred to as ROMS_M, ROMS_F, MIT_M, and MIT_F. Table 1 provides a summary of the resolutions and integration times for the simulations; note that the integration times do not include model spinup.

a. CESM1/POP

POP_C is a global coupled ocean–atmosphere simulation that uses the CESM1 in its preindustrial control configuration (Gent et al. 2011), and POP_M is a global forced ocean-only simulation. The ocean component of POP_C uses a displaced North Pole grid with a nominal 100-km horizontal resolution with the meridional resolution increased to 30 km near the equator. Bathymetry is derived from the ETOPO1 1-min dataset (Amante and Eakins 2009). There are 60 vertical levels in POP_C, with the thickness monotonically increasing from 10 m in the upper ocean to 250 m in the deep ocean with a maximum depth of 5500 m. The vertical grid spacing of POP_M is the same as used in POP_C, but POP_M has two extra layers in the abyssal ocean, extending the maximum depth from 5500 to 6000 m.

In POP_C, the model tracer equations use the Gent and McWilliams (1990) isopycnal transport parameterization. The momentum equations use the anisotropic horizontal viscosity formulation in its generalized form (Smith and McWilliams 2003; Large et al. 2001; Jochum et al. 2008). The vertical mixing is parameterized using the K-profile parameterization (KPP) of Large et al. (1994), as modified by Danabasoglu et al. (2006).

In POP_M, both momentum and tracer equations use biharmonic diffusivities with a cubic dependence on local grid size (Maltrud et al. 1998) and with equatorial values of $27 \times 10^{17}\,\mathrm{m}^4\,\mathrm{s}^{-1}$ for viscosity and $3 \times 10^{17}\,\mathrm{m}^4\,\mathrm{s}^{-1}$ for diffusivity. As in POP_C, vertical mixing coefficients are calculated using the KPP scheme.

POP_M is forced with the Co-ordinated Ocean–Ice Reference Experiments (CORE) repeating annual cycle, that is, normal-year, atmospheric datasets (Large and Yeager 2009). The present simulation uses daily wind stresses incorporating effects of ocean surface currents.

b. ROMS

The ROMS modeling configuration uses a lateral nesting approach consisting of a parent grid at a resolution of 6 km covering most of the Atlantic Ocean (ROMS_M) and a child grid with 2.5 km over the Gulf Stream region (ROMS_F). The nesting procedure is offline and one-way from coarser to finer scales without feedback from the child grid solution onto the parent grid (Penven et al. 2006). ROMS has a vertical terrain-following coordinate system and both domains have 50 levels in the vertical with the same vertical grid system concentrating vertical levels near the surface and bottom as described in Lemarié et al. (2012). Vertical mixing of tracers and momentum is parameterized using KPP (Large et al. 1994). The effect of bottom friction is parameterized through a logarithmic law of the wall with a roughness length $Z_0 = 0.01\,\mathrm{m}$.

Bathymetry for all domains is constructed from the Shuttle Radar Topography Mission (SRTM) 30 plus dataset [Smith and Sandwell (1997); data available online at http://topex.ucsd.edu/WWW_html/srtm30_plus.html]. A Gaussian smoothing kernel with a width of 4 times the topographic grid spacing is used to avoid aliasing whenever the topographic data are available at a higher resolution than the computational grid. Additionally, local smoothing is applied where the steepness of the topography exceeds a 20% gradient.

Boundary conditions for the largest domain (ROMS_M), as well as surface forcings for all simulations are climatological. Boundary data for the largest domain covering the Atlantic Ocean are taken from the monthly averaged SODA ocean climatology (Carton and Giese 2008). Simulations are all forced at the surface by high-frequency winds constructed from a climatology of QuikSCAT scatterometer winds (Risien and Chelton 2008). Heat and freshwater atmospheric forcing are from COADS (da Silva et al. 1994). Freshwater atmospheric forcing has an additional restoring tendency to prevent surface salinity from drifting away from climatological values. This weak restoring is toward climatological monthly surface salinity from the *World Ocean Atlas* (Conkright et al. 2002). A flux correction term is included in heat atmospheric forcing to allow feedback from the ocean to the atmosphere following the formulation of Barnier et al. (1995). More technical details on the configuration may be found in Gula et al. (2015).

c. MITgcm

The MITgcm simulations follow a downscaling approach. Both simulations use 68 layers with cell thickness from a hyperbolic-tangent profile. The minimum thickness is 29 m at the surface and maximum thickness is 212 m at the bottom. Though this minimum thickness near the surface is large, this was allowed in order to maintain less than 100-m thickness down to the depth of the continental shelf. The change in cell thickness occurs between 1000 and 3000 m depth. Bathymetry data are provided from the ETOPO1 1-min dataset (Amante and Eakins 2009), smoothed using a Gaussian filter with a half-width that is twice the grid spacing. As in the POP_M simulation, the bathymetry is approximated through the use of the partial bottom cell representation of Adcroft et al. (1997).

Subgrid-scale processes are parameterized laterally by a Laplacian diffusion in the momentum and tracer equations with lateral eddy viscosity and diffusion coefficients of $20\,\mathrm{m}^2\,\mathrm{s}^{-1}$. Vertical mixing is controlled via the KPP scheme of Large et al. (1994).

Boundary data are derived from the 10-km Hybrid Coordinate Ocean Model (HYCOM) + Navy Coupled Ocean Data Assimilation (NCODA) global assimilative model solutions (experiment GLBa0.08). The HYCOM ocean state is climatologically averaged over the HYCOM model years 2004–08 and detrended to provide climatological boundary conditions. MIT_F utilizes the solution from MIT_M as boundary conditions. Atmospheric forcing for both simulations is supplied from ECMWF ERA-Interim reanalysis, which is also climatologically averaged over the years 2004–08. An atmospheric boundary layer model, Cheap Atmospheric Mixed Layer (CheapAML; Deremble et al. 2013), uses the model state in conjunction with prescribed data to yield heat, salt, and momentum fluxes at the surface.

4. Results

We first begin with a comparison of the Gulf Stream pathway in each model simulation with observations.

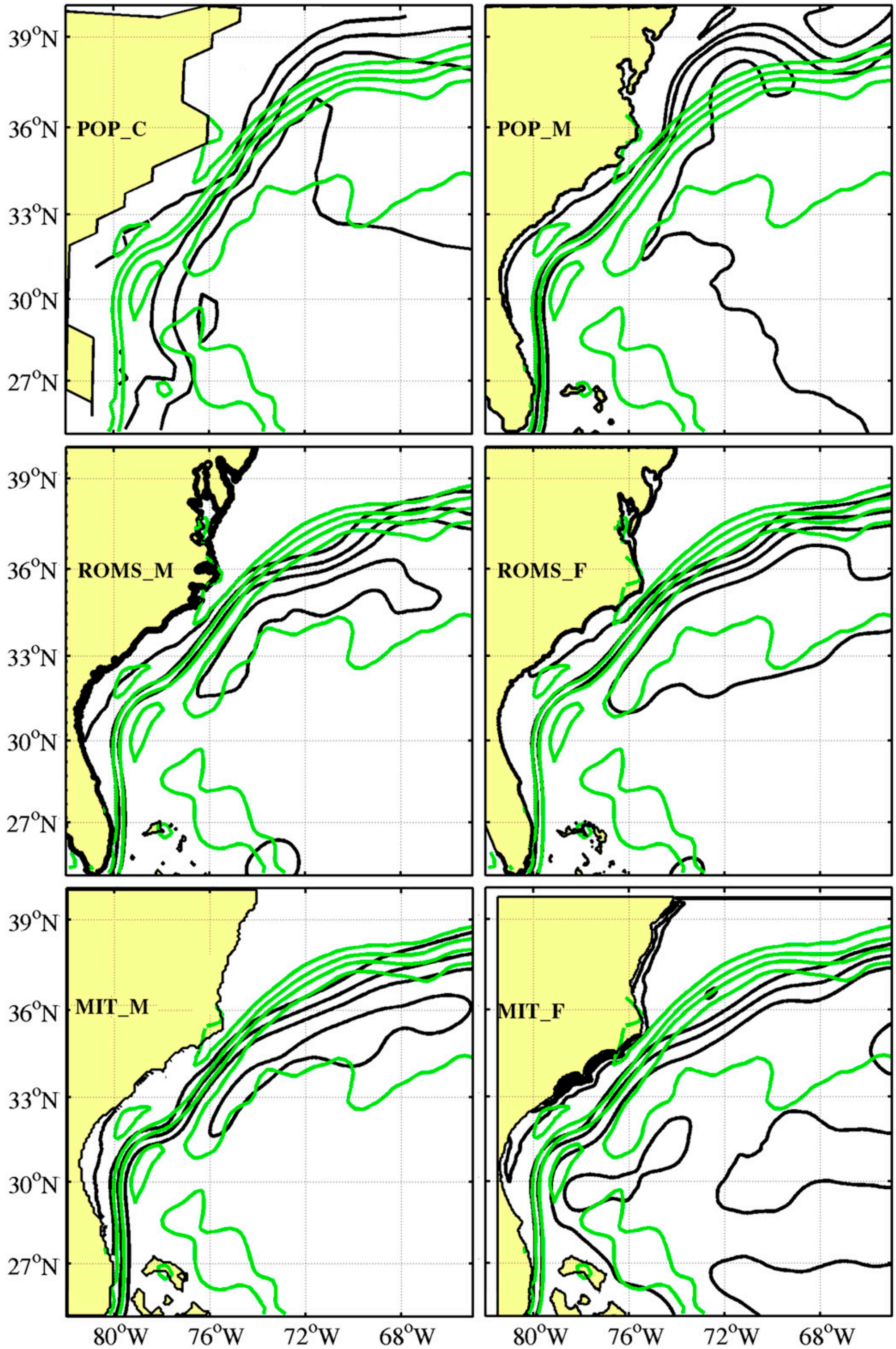

FIG. 1. Five-year average sea surface height observations from AVISO gridded absolute dynamic topography (in green) are shown with each of the model simulations along the southeastern U.S. seaboard. Model and observed sea surface heights are adjusted so that the spatial average (over the region shown) is zero. Contour increments are 0.25 m.

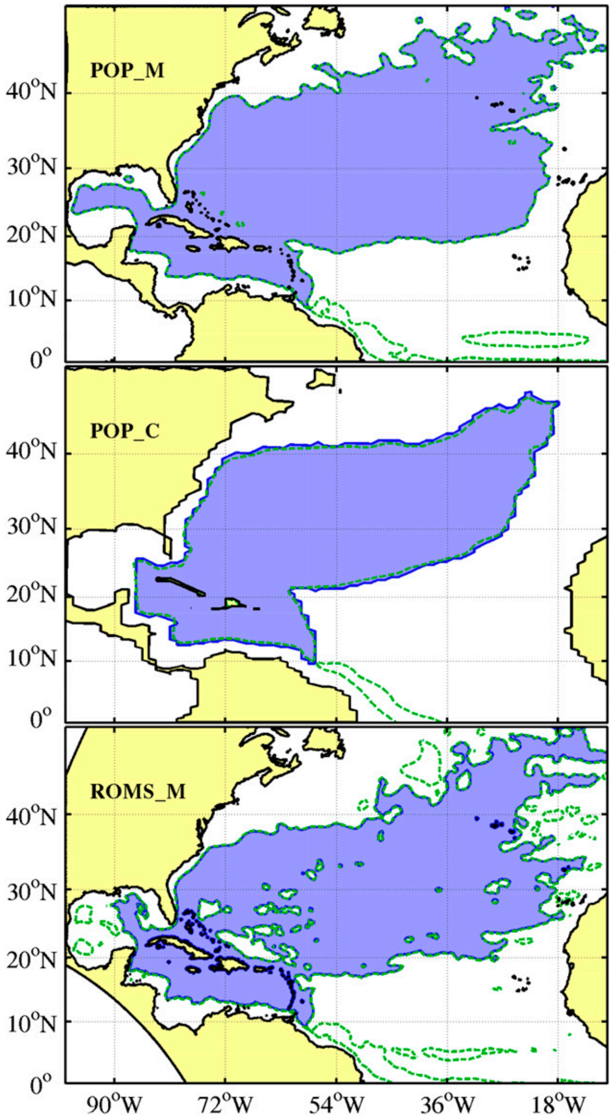

FIG. 2. The regions used for the gyre-integrated budgets are shown shaded in blue for (top) POP_C, (middle) POP_M, and (bottom) ROMS_M. The dashed green line depicts the barotropic streamfunction contour that defines the boundary of the subtropical gyre for each simulation. POP_M and ROMS_M use the 1-Sv contour, and POP_C uses the 10-Sv contour. The 10-Sv contour in POP_C was chosen in order to produce a subtropical gyre region that was similar in geographic location to POP_M and ROMS_M.

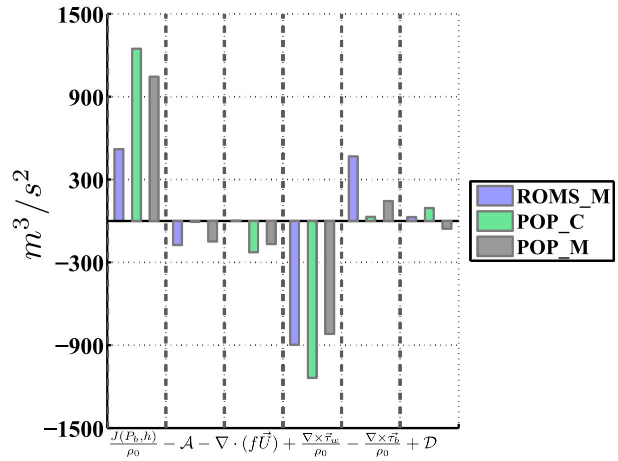

FIG. 3. Time-averaged and gyre-integrated barotropic vorticity budget [Eq. (1)] is shown for ROMS_M, POP_C, and POP_M. The boundary of the gyre for each simulation is shown in Fig. 2. The units are $m^3\,s^{-2}$.

Figure 1 shows the time-averaged free surface height field from each model simulation (in black contours) with time-averaged, gridded AVISO sea surface anomalies from years 2000 to 2005 (in green). All of the fields shown have the spatial average, taken over the depicted region, adjusted to zero. Both POP simulations are shown to produce a Gulf Stream pathway that is north of the observed Gulf Stream past Cape Hatteras between 76° and 68°W. Further, the POP Gulf Streams are shown to remain closer inshore north of Cape Hatteras. The ROMS and MIT simulations show a southward bias from 74° to 68°W but depict a separation occurring closer to Cape Hatteras. We make note of a strong inshore recirculation in the MIT_F simulation. The development of this recirculation, though peculiar, does not produce significant modifications to the Gulf Stream pathway on the continental shelf in comparison to MIT_M. Further, in subsequent vorticity budget analysis, this region is excluded and therefore does not affect budgets in the Gulf Stream.

The simulations POP_C, POP_M, and ROMS_M contain the entire North Atlantic Ocean within the computational domain. For these simulations a representative boundary of the subtropical gyre is chosen by using a closed barotropic streamfunction contour as described in section 2. The contour is chosen for each simulation to yield comparable geographic locations and include the Gulf Stream system. The barotropic streamfunction [$\Psi(x, y)$] is calculated by integrating the meridional transport eastward and specifying $\Psi = 0$ on the coastline of the Americas. For ROMS_M and POP_M, the 1-Sverdrup (Sv; 1 Sv $\equiv 10^6\,m^3\,s^{-1}$) contour is used to define the subtropical gyre. POP_C uses the 10-Sv contour, as this choice yields a geographic region that is similar to ROMS_M and POP_M.

Figure 2 shows the regions that are used to define the gyre for computing the gyre-integrated budgets. The integrated barotropic vorticity budget for these regions is shown in Fig. 3. In each of the POP simulations, the dominant balance is seen to be primarily between the bottom pressure torque and the wind stress curl.

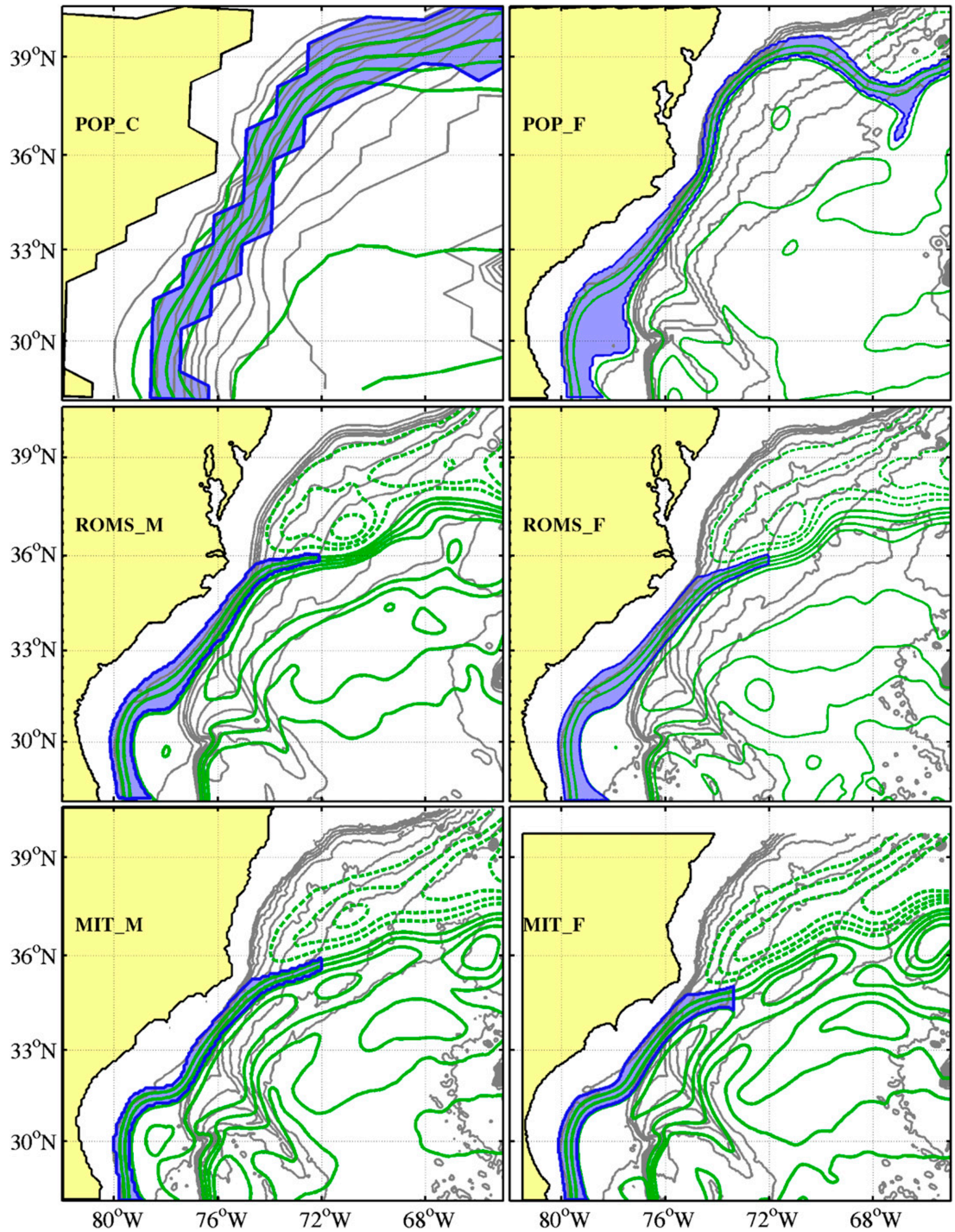

FIG. 4. Gulf Stream region is shown for the (top) POP, (middle) ROMS, and (bottom) MIT simulations. In the MIT and ROMS runs, the Gulf Stream region is defined between the 1- and 30-Sv contours starting just north of the Bahamas and terminating a few degrees east of the separation. In POP_C, the Gulf Stream region is defined between the 10- and 40-Sv contours. All simulations define the 0-Sv contour as the east coast of the United States.

ROMS_C obtains a similar balance with the inclusion of the bottom drag curl. Recall that the bottom drag curl scales against the bottom pressure torque as $h_{ek}/\Delta H$. In the ROMS simulations, additional smoothing is applied to the bathymetry, which is likely to produce bathymetry that is more flat in the open ocean. Because of this, it is possible that $h_{ek}/\Delta H \lesssim 1$, indicating that the bottom drag curl can become important in the interior.

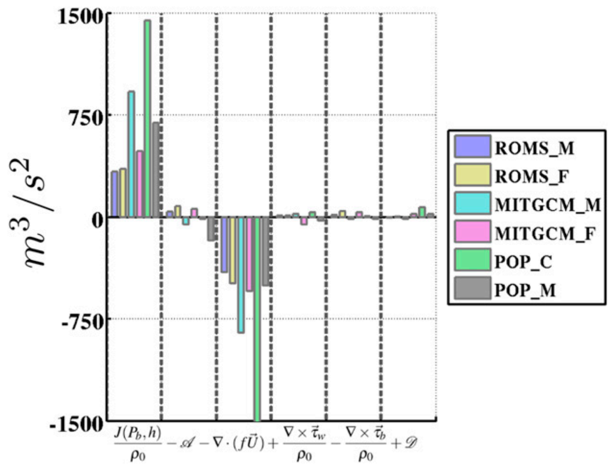

FIG. 5. The time-averaged and Gulf Stream–integrated barotropic vorticity budget is shown for each model simulation using the Gulf Stream regions depicted in Fig. 4. Although the magnitude of each of the terms varies between simulations, the relative contribution of each term within a given simulation is similar.

However, the bottom drag curl in ROMS_M is not found within the Gulf Stream (Fig. 5), indicating that its presence is not required for the usual western boundary current closure, but is instead interpreted as a modification to the interior Sverdrup balance.

The Gulf Stream regions for each of the simulations are shown in Fig. 4. The region is defined between the 1 and 30 Sv contours for all of the runs except POP_C, which uses the 10–40-Sv contours. The southern edge lies at 28°N and the northward extent of the region is chosen to be the location offshore of where the separation occurs. The separation is defined as the location where the barotropic streamfunction crosses the 1200–2000-m isobaths and continues to travel toward deeper locations. Notice that the POP simulations exhibit a Gulf Stream that separates north of the observed separation point at Cape Hatteras (~36°N). Though it is not shown, the resulting budgets were found to be insensitive to changes in the offshore extent of the Gulf Stream region.

Figure 5 shows the barotropic vorticity budget integrated over the regions depicted in Fig. 4. Independent of the model resolution and platform, the leading balance in each run is between the bottom pressure torque and planetary vorticity advection. Notice that in the MITgcm and POP simulations, the bottom pressure torque signal is ~40% larger in the coarser simulation than its higher-resolution counterpart, but this resolution dependence is not observed in the ROMS simulations. The reason for such a distinction in the POP and MITgcm simulations is unclear, though we point out distinctions in the modeling approaches that may be responsible. At higher resolutions, smaller-scale structure in the bathymetry is resolved and is able to imprint these details on the ocean state. In transitioning from MIT_M to MIT_F (and similarly for POP_C to POP_M), there is a more substantial introduction of finescale structure in the bathymetry than from ROMS_M to ROMS_F, where we recall that the ROMS configurations employ a more aggressive smoothing in the bathymetry (see section 3). The overestimation of the bottom pressure torque in the coarser z-coordinate models (POP and MITgcm) can possibly be linked to the discrete and finite number of bathymetric gradients that can be represented with such a vertical discretization. Interestingly, as more structure is included in the bathymetry, the net bottom pressure torque signal in the Gulf Stream is shown to decrease in the MIT and POP simulations as resolution is increased. From the budgets shown, it is reasonable to suspect that the MIT and POP signals are approaching values closer to those obtained in the ROMS simulations with increasing resolution, suggesting that the overestimation of the bottom pressure torque is part of a discretization error within z-coordinate models. Despite these detailed differences between the presented simulations, the relative balances are similar in an integrated view of the Gulf Stream.

Figure 6 shows the bottom pressure torque signal for the MIT and ROMS simulations on the continental shelf. The signal is smoothed in each simulation using a Gaussian filter with a half-width of 20 km. Notice that in both models, the fine-resolution simulations reveal the emergence of a more detailed structure of the bottom pressure torque signal over the Charleston Bump (31°N, 76°W). This signal is linked to the more detailed representation of the bathymetric feature that can modify the net integrated balance over the Gulf Stream. ROMS_M shows a weaker signal in the bottom pressure torque over the continental shelf. This is due to the weaker bathymetric slopes caused by the smoothing process used in constructing the bathymetry fields. Nonetheless, the integrated balances within each simulation produce similar relative balances. The emergence of the detailed structure in the bottom pressure torque signal is qualitatively similar between the ROMS and MITgcm simulations, suggesting that vorticity balances are robust.

When comparing the Gulf Stream and gyre budgets, notice that almost all of the bottom pressure torque signal in the gyre budget is accounted for within the Gulf Stream region (Figs. 3, 5). By mass conservation, the observed planetary vorticity advection in the Gulf Stream must be equal and opposite to that found in the interior of the gyre. Thus, the emerging picture of the gyre is one that receives anticyclonic vorticity in the interior that is balanced by cyclonic vorticity production

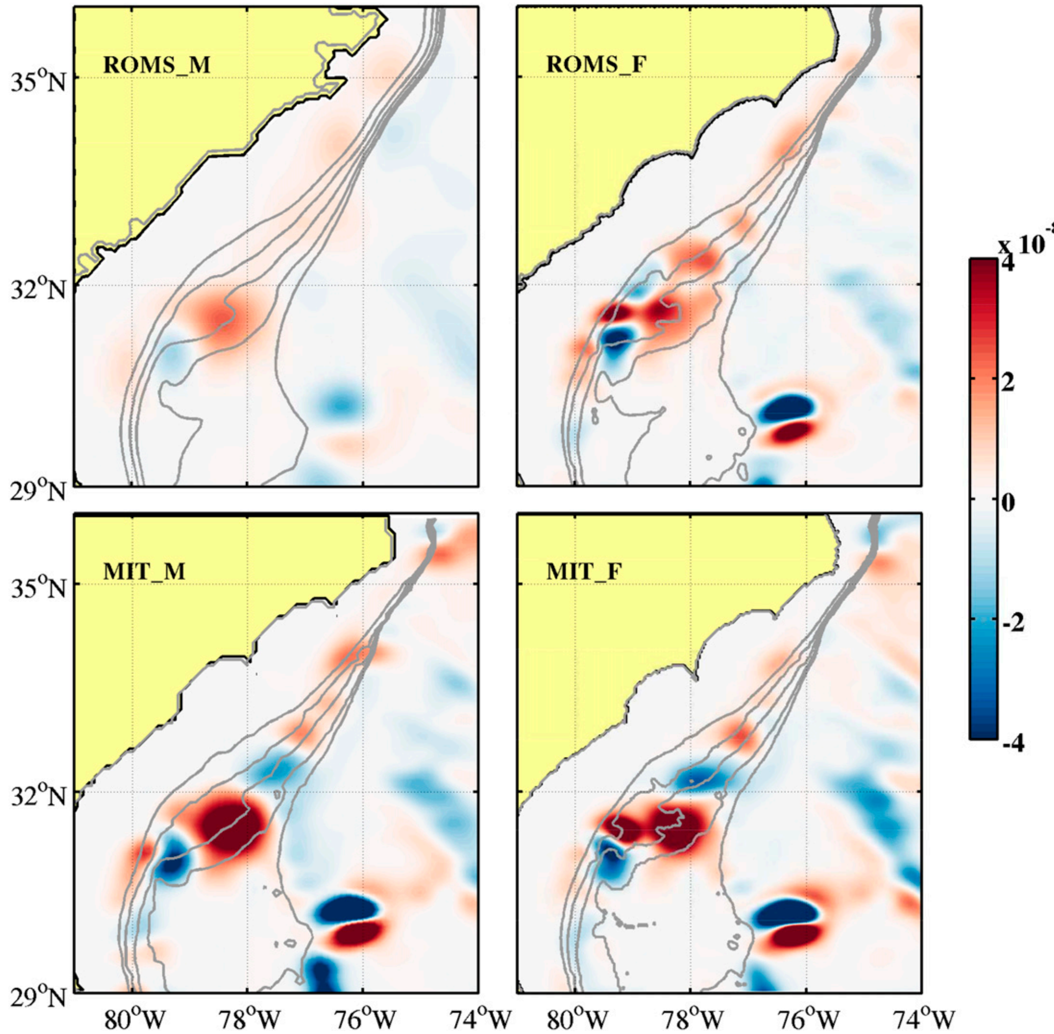

FIG. 6. Bottom pressure torque is shown for the MIT and ROMS simulations zoomed in over the Charleston Bump. All figures have been smoothed to with a Gaussian filter of half-width, $h_w \approx 20$ km. Isobaths are shown from 0 to 1000 m in 200-m increments.

within the western boundary current through the bottom pressure torque. This result is in agreement with previous studies by Hughes and DeCuevas (2001), which provides further evidence for the robustness of the inviscid gyre. Despite these agreements, it is clear that the gyre structure, particularly the Gulf Stream separation, varies between model simulations (Fig. 4).

The northerly separation observed in the POP simulations, depicted in the upper panels of Fig. 4, is an unfavorable representation of the Gulf Stream, as it can lead to warm SST biases in the Mid-Atlantic Bight (Gent et al. 2011). From the scale analysis in section 2b and the presented budgets, it should be clear that the separation location is not linked to large-scale balances. Instead, the separation behavior is directly related to the local vorticity balances, contrary to the classic wind-driven gyre framework of Stommel (1948) and Munk (1950). In POP_M, the Laplacian and biharmonic viscosity coefficients are (to an order of magnitude) $A_h \approx 10^3\,\mathrm{m^2\,s^{-1}}$ and $A_{4h} \approx 10^{17}\,\mathrm{m^4\,s^{-1}}$. As in section 2b, the Laplacian and biharmonic length scales ($L_{\mathrm{visc}} \approx 1$ km and $L_{A4} \approx 100$ km) suggest that the biharmonic and bottom pressure torque are comparable in magnitude on length scales at or smaller than 100 km.

Figure 7 depicts the vorticity budget in field plots over the Gulf Stream region for each of the simulations. For clarity, all of the terms are smoothed with a Gaussian filter of half-width $h_w = 20$ km (except POP_C). The left-most column shows the sum of the inviscid and frictionless torque (bottom pressure torque, nonlinear torque, planetary vorticity advection, and wind stress curl) and each column to the right shows the lateral

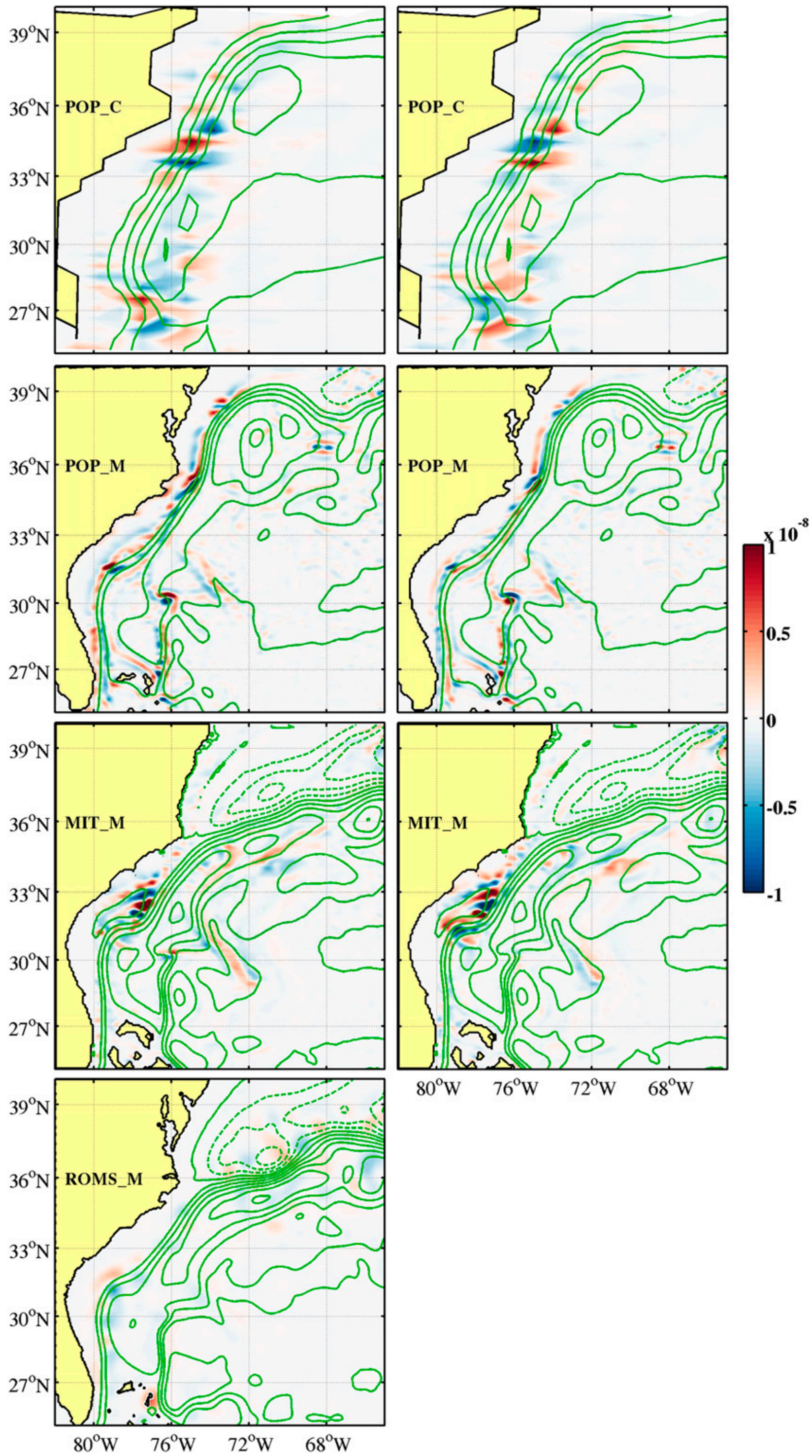

FIG. 7. (left) The sum of bottom pressure torque, nonlinear torque, planetary vorticity advection, and wind stress curl is shown for each of the six simulations. (right) The lateral viscous torque is shown in for the POP_C, POP_M, and MIT_M simulations. In the ROMS_M and MIT_M simulations, notice that only a significant signal remains around the Charleston Bump (~32°N, 78°W) after adding all of the frictionless and inviscid terms. In the POP simulations, viscous or frictional torque is still required throughout the Gulf Stream, particularly around Cape Hatteras. The details of the lateral viscous torque observed in the MITgcm simulations are addressed in Fig. 8. Although not shown, a similar result is found for the fine-resolution simulations.

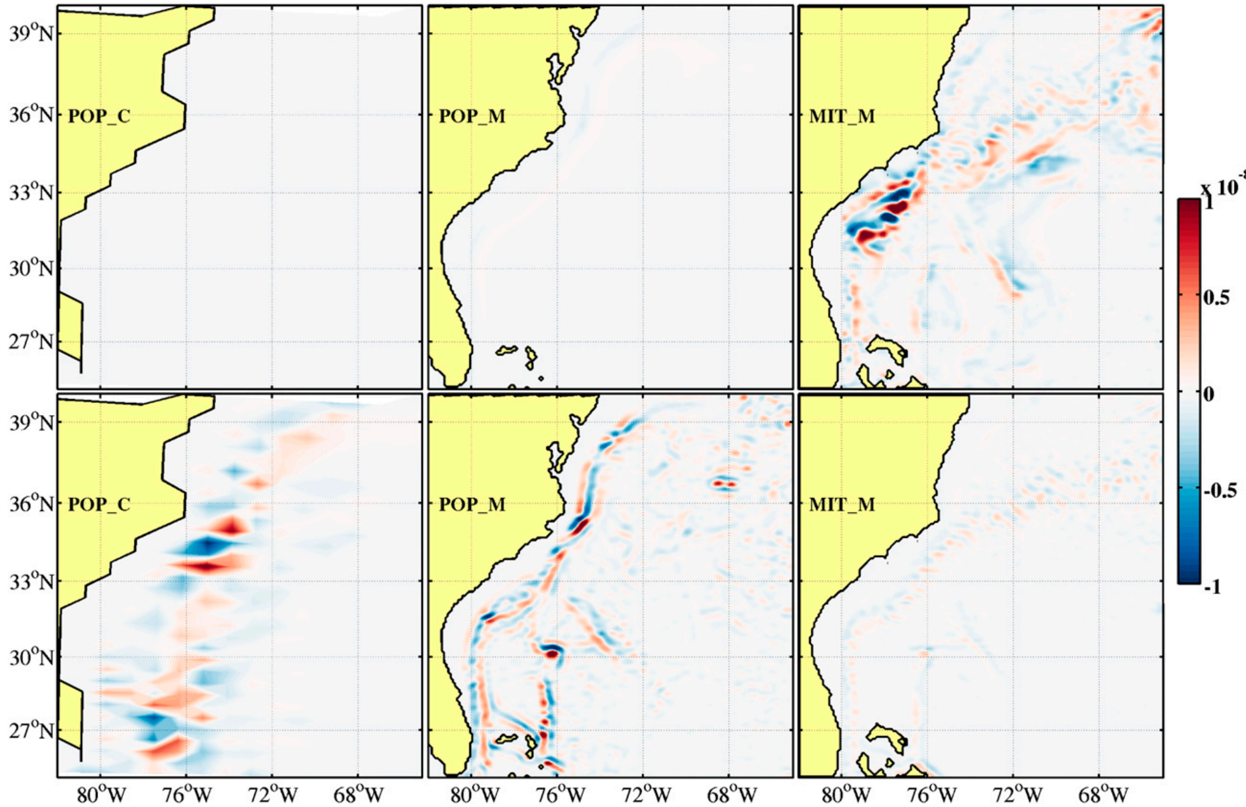

FIG. 8. (top) The wind stress curl and (bottom) the wind stress curl plus the lateral viscous torque for (left) POP_C, (center) POP_M, and (right) MIT_M. The wind stress curl is considerably stronger in MIT_M and is shown to almost completely cancel with the lateral viscous torque.

viscous torque for the MITgcm and POP simulations. Focusing on Cape Hatteras (~36°N), both POP simulations are shown to require lateral viscous torque to close the vorticity budget. Although the MITgcm simulations appear to also require lateral viscous torque, particularly around the Charleston Bump (~32°N, 78°W), there is an independent balance between the lateral viscous torque and the wind stress curl (Fig. 8). The top row in Fig. 8 shows the wind stress curl for the POP simulations and MIT_M. It is clear that MIT_M exhibits a wind stress curl signal that is larger than in the POP simulations, particularly over the Charleston Bump. Adding together the wind stress curl and the lateral viscous torque (shown in the bottom row of Fig. 8) illustrates an almost complete cancellation in these two terms in MIT_M. This particular aspect of the MITgcm simulation is linked to the use of the CheapAML atmospheric boundary model, which takes into account the ocean surface state in momentum and buoyancy fluxes. Notice that the largest wind stress curl signals lie within the Gulf Stream pathway, particularly over the Charleston Bump, where there is significant variability in the sea surface state because of eddy activity. Though not the focus of this project, it is seen that the inclusion the ocean state in flux calculations can yield vorticity sources that are an order of magnitude different than ocean models with a prescribed flux. Interestingly, this attribute does not modify the overall vorticity budget for the Gulf Stream and does not seem to upset the local inviscid balances.

Given that the integrated budgets reveal the inviscid balance across resolution and model platform, it is concluded that the bottom pressure torque closure is a qualitatively robust solution. This persists into POP_C, emphasizing that there is considerable dynamical consistency in the coarse-resolution models. Despite the agreement in the integrated budgets, the differences in the Gulf Stream separation are consistent with the hypothesis that the separation relies on local dynamics. In the POP simulations, the Gulf Stream is found to separate unfavorably north of Cape Hatteras and is characterized by a vorticity balance in which viscous torque are important locally. The ROMS and MIT simulations, which model a Gulf Stream that separates closer to Cape Hatteras, show an almost complete vorticity balance without the need for viscous torque. This suggests that, although the large-scale budgets are accurate in the POP simulations, the smaller-scale intrusion of viscous dynamics are associated with the northward separation of the Gulf Stream.

Acknowledgments. This research was conducted under the National Science Foundation Grants OCE-1049131 (FSU and UCLA) and OCE-1049190 (NCAR) in support of the Earth System Models (EaSM) program. Yeager was supported by the NOAA Climate Program Office under Climate Variability and Predictability Program Grants NA09OAR4310163 and NA13OAR4310138, and by the National Science Foundation Collaborative Research EaSM2 Grant OCE-1243015. Bates was supported by the Regional and Global Climate Modeling Program (RGCM) of the U.S. Department of Energy, Office of Science (BER), Cooperative Agreement DE-FC02-97ER62402.

REFERENCES

Adcroft, A., C. Hill, and J. Marshall, 1997: Representation of topography by shaved cells in a height coordinate ocean model. *Mon. Wea. Rev.*, **125**, 2293–2315, doi:10.1175/1520-0493(1997)125<2293:ROTBSC>2.0.CO;2.

Amante, C., and B. Eakins, 2009: ETOPO1 1 Arc-Minute Global Relief Model: Procedures, data sources and analysis. NOAA Tech. Memo. NESDIS NGDC-24, NOAA/National Geophysical Data Center, accessed 3 December 2015, doi:10.7289/V5C8276M.

Barnier, B., L. Siefried, and P. Marchesiello, 1995: Thermal forcing for a global ocean circulation model using a three-year climatology of ECMWF analyses. *J. Mar. Syst.*, **6**, 363–380, doi:10.1016/0924-7963(94)00034-9.

Bryan, F. O., M. Hecht, and R. Smith, 2007: Resolution convergence and sensitivity studies with North Atlantic circulation models. Part I: The western boundary current system. *Ocean Modell.*, **16**, 141–159, doi:10.1016/j.ocemod.2006.08.005.

Carton, J., and B. Giese, 2008: A reanalysis of ocean climate using Simple Ocean Data Assimilation (SODA). *Mon. Wea. Rev.*, **136**, 2999–3017, doi:10.1175/2007MWR1978.1.

Chassignet, E., and D. Marshall, 2008: Gulf stream separation in numerical ocean models. *Ocean Modeling in an Eddying Regime*, *Geophys. Monogr.*, Vol. 177, Amer. Geophys. Union, 39–61.

Conkright, M., R. Locarnini, H. Garcia, T. O'Brien, T. Boyer, C. Stephens, and J. Antonov, 2002: *World Ocean Atlas 2001*: Objective analyses, data statistics and figures. CD-ROM documentation, National Oceanographic Data Center, 17 pp. [Available online at http://odv.awi.de/fileadmin/user_upload/odv/data/WOA01/README.PDF.]

Danabasoglu, G., W. Large, J. Tribbia, P. Gent, B. Briegleb, and J. McWilliams, 2006: Diurnal coupling in the tropical oceans of CCSM3. *J. Climate*, **19**, 2347–2365, doi:10.1175/JCLI3739.1.

da Silva, A., C. Young, and S. Levitus, 1994: *Algorithms and Procedures*, Vol. 1, *Atlas of Surface Marine Data 1994*, NOAA Atlas NESDIS 6, 74 pp.

Deremble, B., N. Wienders, and W. Dewar, 2013: CheapAML: A simple, atmospheric boundary layer model for use in ocean-only model calculations. *Mon. Wea. Rev.*, **141**, 809–821, doi:10.1175/MWR-D-11-00254.1.

Gent, P., and J. McWilliams, 1990: Isopycnal mixing on ocean circulation models. *J. Phys. Oceanogr.*, **20**, 150–155, doi:10.1175/1520-0485(1990)020<0150:IMIOCM>2.0.CO;2.

——, and Coauthors, 2011: The Community Climate System Model version 4. *J. Climate*, **24**, 4973–4991, doi:10.1175/2011JCLI4083.1.

Gula, J., J. Molemaker, and J. McWilliams, 2015: Gulf Stream dynamics along the southeastern U.S. seaboard. *J. Phys. Oceanogr.*, **45**, 690–715, doi:10.1175/JPO-D-14-0154.1.

Haidvogel, D., J. McWilliams, and P. Gent, 1992: Boundary current separation in a quasigeostrophic, eddy-resolving ocean circulation model. *J. Phys. Oceanogr.*, **22**, 882–902, doi:10.1175/1520-0485(1992)022<0882:BCSIAQ>2.0.CO;2.

Holland, W., 1973: Baroclinic and topographic influences on the transport in western boundary currents. *Geophys. Fluid Dyn.*, **4**, 336–354, doi:10.1080/03091927208236095.

Hughes, C., 2000: A theoretical reason to expect inviscid western boundary currents in realistic oceans. *Ocean Modell.*, **2**, 73–83, doi:10.1016/S1463-5003(00)00011-1.

——, and B. DeCuevas, 2001: Why western boundary currents in realistic oceans are inviscid: A link between form stress and bottom pressure torques. *J. Phys. Oceanogr.*, **31**, 2871–2885, doi:10.1175/1520-0485(2001)031<2871:WWBCIR>2.0.CO;2.

Hughes, R., 1986: On the role of criticality in coastal flows over irregular bottom topography. *Dyn. Atmos. Oceans*, **10**, 129–147, doi:10.1016/0377-0265(86)90003-5.

Jackson, L., C. Hughes, and R. Williams, 2006: Topographic control of basin and channel flows: The role of bottom pressure torques and friction. *J. Phys. Oceanogr.*, **36**, 1786–1805, doi:10.1175/JPO2936.1.

Jochum, M., G. Danabasoglu, M. Holland, Y. Kwon, and W. Large, 2008: Ocean viscosity and climate. *J. Geophys. Res.*, **113**, C06017, doi:10.1029/2007JC004515.

Large, W., and S. Yeager, 2009: The global climatology of an interannually varying air-sea flux data set. *Climate Dyn.*, **33**, 341–364, doi:10.1007/s00382-008-0441-3.

——, J. McWilliams, and S. Doney, 1994: Oceanic vertical mixing: A review and a model with a nonlocal boundary layer parameterization. *Rev. Geophys.*, **32**, 363–403, doi:10.1029/94RG01872.

——, G. Danabasoglu, J. McWilliams, P. Gent, and F. Bryan, 2001: Equatorial circulation in a global ocean climate model with anisotropic horizontal viscosity. *J. Phys. Oceanogr.*, **31**, 518–536, doi:10.1175/1520-0485(2001)031<0518:ECOAGO>2.0.CO;2.

Lemarié, F., J. Kurian, A. Shchepetkin, M. Molemaker, F. Colas, and J. McWilliams, 2012: Are there inescapable issues prohibiting the use of terrain-following coordinates in climate models? *Ocean Modell.*, **42**, 57–79, doi:10.1016/j.ocemod.2011.11.007.

Maltrud, M., R. Smith, A. Semtner, and R. Malone, 1998: Global eddy resolving ocean simulations driven by 1985-1995 atmospheric fields. *J. Geophys. Res.*, **103**, 30 825–30 853, doi:10.1029/1998JC900013.

Marshall, J., C. Hill, L. Perelman, and A. Adcroft, 1997: Hydrostatic, quasi-hydrostatic, and non-hydrostatic ocean modelling. *J. Geophys. Res.*, **102**, 5733–5753, doi:10.1029/96JC02776.

Munk, W., 1950: On the wind-driven ocean circulation. *J. Meteor.*, **7**, 79–93, doi:10.1175/1520-0469(1950)007<0080:OTWDOC>2.0.CO;2.

Penven, P., L. Debreu, P. Marchesiello, and J. McWilliams, 2006: Application of ROMS embedding procedure for the central California upwelling system. *Ocean Modell.*, **12**, 157–187, doi:10.1016/j.ocemod.2005.05.002.

Risien, C., and D. Chelton, 2008: A global climatology of surface wind and wind stress fields from eight years of QuikSCAT scatterometer data. *J. Phys. Oceanogr.*, **38**, 2379–2413, doi:10.1175/2008JPO3881.1.

Shchepetkin, A., and J. McWilliams, 2005: The Regional Ocean Modeling System (ROMS): A split-explicit, free-surface, topography-following-coordinate ocean model. *Ocean Modell.*, **9**, 347–404, doi:10.1016/j.ocemod.2004.08.002.

Smith, R. D., and J. McWilliams, 2003: Anisotropic horizontal viscosity for ocean models. *Ocean Modell.*, **5**, 129–156, doi:10.1016/S1463-5003(02)00016-1.

——, and Coauthors, 2010: The Parallel Ocean Program (POP) reference manual: Ocean component of the Community Climate System Model (CCSM) and Community Earth System Model (CESM). LANL Doc., 140 pp [Available online at http://www.cesm.ucar.edu/models/cesm1.0/pop2/doc/sci/POPRefManual.pdf.]

Smith, W. H. F., and D. T. Sandwell, 1997: Global sea floor topography from satellite altimetry and ship depth soundings. *Science*, **277**, 1956–1962, doi:10.1126/science.277.5334.1956.

Stern, M., 1998: Separation of a density current from the bottom of a continental shelf. *J. Phys. Oceanogr.*, **28**, 2040–2049, doi:10.1175/1520-0485(1998)028<2040:SOADCF>2.0.CO;2.

Stommel, H., 1948: The westward intensification of wind-driven ocean currents. *Eos, Trans. Amer. Geophys. Union*, **29**, 202–206, doi:10.1029/TR029i002p00202.

Talandier, C., and Coauthors, 2014: Improvements of simulated western North Atlantic current system and impacts on the AMOC. *Ocean Modell.*, **76**, 1–19, doi:10.1016/j.ocemod.2013.12.007.